






Thermal degradation of optical resonances in plasmonic nanoparticles

Lasse K. Sørensen, ^{a,b} Daniil E. Khrennikov,^a Valeriy S. Gerasimov, ^{*a,c}
Alexander E. Ershov,^{a,c} Maxim A. Vysotin,^{a,d} Susanna Monti, ^e
Vadim I. Zakomirnyi, ^{a,c} Sergey P. Polyutov,^{*a,f} Hans Ågren ^{a,g} and
Sergey V. Karpov^{a,d}

The dependence of plasmon resonance excitations in ultrafine (3–7 nm) gold nanoparticles on heating and melting is investigated. An integrated approach is adopted, where molecular dynamics simulations of the spatial and temporal development of the atoms constituting the nanoparticles generate trajectories out of which system conformations are sampled and extracted for calculations of plasmonic excitation cross sections which then are averaged over the sample configurations for the final result. The calculations of the plasmonic excitations, which take into account the temperature- and size-dependent relaxation of the plasmons, are carried out with a newly developed Extended Discrete Interaction Model (EXDIM) and complemented by multilayered Mie theory. The integrated approach clearly demonstrates the conditions for suppression of the plasmons starting at temperatures well below the melting point. We have found a strong inhomogeneous dependence of the atom mobility in the particle crystal lattice increasing from the center to its surface upon the temperature growth. The plasmon resonance suppression is associated with an increase of the mobility and in the amplitude of phonon vibrations of the lattice atoms accompanied by electron–phonon scattering. This leads to an increase in the relaxation constant impeding the plasmon excitation as the major source of the suppression, while the direct contribution from the increase in the lattice constant and its chaotization at melting is found to be minor. Experimental verification of the suppression of surface plasmon resonance is demonstrated for gold nanoparticles on a quartz substrate heated up to the melting temperature and above.

Received 30th September 2021,

Accepted 2nd December 2021

DOI: 10.1039/d1nr06444d

rs.c.li/nanoscale

The interaction of metal nanoparticles with laser radiation is a phenomenon that is as intriguing as it is important in research areas covering plasmonics.^{1–7} The study of such processes is thus of topical interest for nanosensorics,^{8–10} nanobiomedicine and biotechnology¹¹ as well as for energy harvesting,¹² wave guiding and near-field heat transfer,^{13–15} all relying on the strong field and energy concentration generated by

plasmonic excitations in nanoparticles. Despite the fact that the fundamental processes in plasmonics nowadays are quite well characterized, there is still a considerable lack of understanding of the effects of light–matter interaction when plasmonic nanoparticles are exposed to high-intensity pulsed laser radiation.^{16–21} This situation is unfortunate considering that the photothermal properties of plasmonic nanoparticles are associated with important applications, for instance when the particles are bound to malignant cell membranes or malignant neoplasms, where hydrodynamic effects accompanying the vaporization process from heated nanoparticles gain therapeutic effects. Damage of the malignant cell membrane is realized through the heating by pulsed laser radiation of the nanoparticles which at the initial moment of the bubble nucleation creates a wave of high pressure acting on the membrane. In this case, the value of pressure, considerably exceeding the threshold values, gives an indication of irreversible cell damage. Related, important, applications of plasmonic nanoparticles in anticancer therapy refer to hyperthermia of malignant cells in pulsed laser fields.²² These are a few of a number of applications of the heating of nanoparticles by laser radi-

^aInternational Research Center of Spectroscopy and Quantum Chemistry – IRC SQC, Siberian Federal University, Krasnoyarsk, 660041, Russia.

E-mail: spolyutov@sfu-kras.ru, gerasimov@icm.krasn.ru

^bDepartment of Theoretical Chemistry and Biology, Royal Institute of Technology, Stockholm, SE-10691, Sweden

^cInstitute of Computational Modeling, Federal Research Center KSC SB RAS, Krasnoyarsk, 660036, Russia

^dL. V. Kirensky Institute of Physics, Federal Research Center KSC SB RAS, Krasnoyarsk, 660036, Russia

^eCNR-ICCOM, Institute of Chemistry of Organometallic Compounds, via G. Moruzzi 1, I-56124 Pisa, Italy

^fFederal Siberian Research Clinical Centre under FMBA of Russia, 660037, Kolomenskaya, 26 Krasnoyarsk, Russia

^gDepartment of Physics and Astronomy, Uppsala University, Box 516, SE-751 20 Uppsala,

ation, see reviews in.^{7,23–25} However, in some of these applications the effect of heating on the optical properties of the nanoparticles and *vice versa* are often not taken into account.

A special case of the photothermal processes takes place at high temperatures when the plasmonic nanoparticles undergo a transition into the liquid state²⁶ as studied in papers^{27–29} focusing on the influence of pulsed laser radiation on plasmonic nanoparticle aggregates. Here the effect of melting of nanoparticles on their resonant properties was shown to generate changes in the optical properties and in particular non-linear optical responses of such systems due to the pulsed laser fields.³⁰ However, the photothermal and optical properties of nanoparticles under laser pulses cannot be predicted with their temperature-independent optical absorption cross section. Besides, the thermal properties of the ambient liquid at high temperatures and possible melting of nanoparticles are side effects that need to be taken into account.²² For instance, in areas like plasmonic enhanced infrared energy harvesting, using cascade upconversion amplification,³¹ the problem of melting due to the ultra-enhanced fields becomes crucial.

Motivated by these endeavors, our present work aims to establish the correlation between the optical properties of plasmonic nanoparticles and structural properties of their crystal lattices in a wide range of temperature variation, taking into account the temperature dependence of the particle structure as well as of the relaxation constant.

1. Models and methods

1.1. Extended discrete interaction model

The Extended Discrete Interaction Model (Ex-DIM),^{32,33} is a discrete structure model parameterized directly from experimental data. In this model each atom is represented by a Gaussian charge distribution and endowed with a polarizability and relaxation constants which governs the inter-atomic interaction.^{34–37} Ex-DIM has shown to improve the description of the surface topology, geometric dependence in comparison to older Discrete Interaction Models.³² Since it previously has been described in detail we will here only focus on the improvements in the model preceding this study.

The frequency dependent polarizabilities from the fluctuating dipoles $\boldsymbol{\mu}$ are determined by applying a weak uniform electric field \mathbf{E} :

$$\mathbf{A}\boldsymbol{\mu} = \mathbf{E}. \quad (1)$$

Here \mathbf{A} is defined as:

$$\mathbf{A}_{ij} = \delta_{ij}\alpha_{ij}^{-1} - (1 - \delta_{ij})\mathbf{T}_{ij}^{(2)} \quad (2)$$

where $\mathbf{T}_{ij}^{(2)}$ is the electrostatic interaction tensor between dipoles³⁸ and α_{ij} is defined as:

$$\alpha_{ii,kl}(\omega, \mathbf{P}, T, f_{\text{cn}}) = \left(\frac{R_i(f_{\text{cn}})}{R_{i,\text{bulk}}} \right)^3 \alpha_{i,s,kl} L(\omega, \mathbf{P}, T). \quad (3)$$

In eqn (3), $R_{i,\text{bulk}}$ is the bulk radius of the atom, $R_i(f_{\text{cn}})$ the coordination number (f_{cn})³⁹ scaled radius,³² $\alpha_{i,s,kl}$ is the

assigned atomic polarizability and $L(\omega, \mathbf{P}, T)$ a size- and temperature-dependent Lorentzian.

Here $\alpha_{i,s,kl}$ used to be the static atomic polarizability³² but we found that employing the static atomic polarizability greatly overestimates both the total polarizability and extinction cross section comparing to classic methods when reasonable values for the relaxation constants were utilized. This finding is in line with the density functional theory (DFT) calculations on smaller gold clusters where the polarizability per atom decreases significantly with cluster size.^{40,41} The fitting of the Ex-DIM parameters from experiment is discussed in Appendix A.

The geometric dependence of the surface plasmon resonance is determined by the size- and temperature-dependent Lorentzian $L(\omega, \mathbf{P}, T)$:

$$L(\omega, \mathbf{P}, T) = N(L_x(\omega, P_x, T) + L_y(\omega, P_y, T) + L_z(\omega, P_z, T)), \quad (4)$$

where each Lorentzian:

$$L_i(\omega, P_i, T) = \frac{1}{\omega_i^2(P_i) - \omega^2 - i\Gamma_i(P_i, T)\omega}, \quad (5)$$

depends on the frequency ω , the plasmon length P_i ⁴² and the temperature T . The plasmon length is defined as the maximum distance between two atoms plus the radius of those atoms in the given direction, in other words – the length over which the oscillations take place. The size-dependent frequency $\omega_i(P_i)$ is defined as:

$$\omega_i(P_i) = \omega_a(1 + A_s/P_i), \quad (6)$$

where ω_a and A_s are a chemical element specific resonance frequency and a size dependence quantity, respectively, which are fitted from experiment, see Appendix A.

The extinction cross section σ_{ext} is calculated using the following relation:

$$\sigma_{\text{ext}} = 4\pi|\mathbf{k}| \frac{\Im(\boldsymbol{\mu} \cdot \mathbf{E}_0^*)}{|\mathbf{E}_0|^2}, \quad (7)$$

where \mathbf{k} is the wave vector, \mathbf{E}_0 is the external field and $\boldsymbol{\mu}$ the fluctuating dipoles. The extinction efficiency Q_{ext} of a nanoparticle is given by

$$Q_{\text{ext}} = \sigma_{\text{ext}}/(\pi R^2). \quad (8)$$

1.1.1. Size- and temperature-dependent relaxation constants. In previous applications of the Ex-DIM the relaxation constant Γ was a fixed quantity.³² However, in order to describe both the dampening and broadening of the plasmon resonance with respect to temperature due to scattering of electron-phonons and lattice defects and due to the finite size effect in a particle with radius R_i , the relaxation constant will now be written as a sum of a size- and temperature-dependent relaxation contributions:

$$\Gamma_i(P_i, T) = \Gamma(P_i) + \Gamma_{\text{e-ph,d}}(T). \quad (9)$$

The size-dependent relaxation constant $\Gamma(P_i)$:

$$\Gamma(P_i) = K_s/P_i \quad (10)$$

is proportional to the inverse plasmon length and is therefore mostly relevant for particles of small size and K_s is here a chemical element specific constant. The size-dependent relaxation in the Ex-DIM has in this way the same functional form as the size-dependence of the resonance frequency and the size-dependent relaxation constant from classical models as seen in eqn (18).

The phonon spectrum and the temperature dependence of the relaxation constant can be derived from the Debye model for as:^{26,43}

$$\Gamma_{e-ph,d}(T) = K_0 T^5 \int_0^{T_D/T} \frac{z^4 dz}{e^z - 1} \quad (11)$$

where T_D is the Debye temperature and K_0 is a constant including the total scattering cross section of an isolated atom, the ion mass, the ion density, the Debye wave number, the Debye temperature, and other universal constants. K_0 can be found using already determined $\Gamma_{e-ph,d}(T_m)$ values, where T_m is the melting temperature. Upon melting, the specific resistance of gold exhibits a sharp jump of 2.4 times in comparison to the solid resulting in the change of the relaxation constant:²⁶

$$\Gamma_{e-ph,d}^{(l)}(T_m) = 2.4 \cdot \Gamma_{e-ph,d}^{(s)}(T_m), \quad (12)$$

where l and s denote here the liquid and solid phase, respectively.

1.1.2. Melting temperature in Ex-DIM. In Ex-DIM the melting temperature is calculated from the plasmon length

$$\begin{aligned} d_n^j m_{j-1} \psi'_n(m_j x_{j-1}) - g_n^j m_{j-1} \chi'_n(m_j x_{j-1}) - d_n^{j-1} m_j \psi'_n(m_{j-1} x_{j-1}) + g_n^{j-1} m_j \chi'_n(m_{j-1} x_{j-1}) &= 0 \\ d_n^j \psi_n(m_j x_{j-1}) - g_n^j \chi_n(m_j x_{j-1}) - d_n^{j-1} \psi_n(m_{j-1} x_{j-1}) + g_n^{j-1} \chi_n(m_{j-1} x_{j-1}) &= 0 \\ e_n^j m_{j-1} \psi'_n(m_j x_{j-1}) - f_n^j m_{j-1} \chi'_n(m_j x_{j-1}) - e_n^{j-1} m_j \psi'_n(m_{j-1} x_{j-1}) + f_n^{j-1} m_j \chi'_n(m_{j-1} x_{j-1}) &= 0 \\ e_n^j \psi_n(m_j x_{j-1}) - f_n^j \chi_n(m_j x_{j-1}) - e_n^{j-1} \psi_n(m_{j-1} x_{j-1}) + f_n^{j-1} \chi_n(m_{j-1} x_{j-1}) &= 0 \end{aligned} \quad (15)$$

using the generalised Gibbs–Thomson equation:⁴⁴

$$0 = L_m \left(\frac{T_m}{T_m^*} - 1 \right) + \Delta c \left[T_m \ln \left(\frac{T_m}{T_m^*} \right) + T_m^* - T_m \right] + \frac{2\sigma_{sl}\kappa}{\rho_s}, \quad (13)$$

where the effect of pressure is omitted. In eqn (13) L_m is the latent heat in the phase change for melting, T_m the temperature at which the phase change occurs (in the case of a curved surface of a body), T_m^* the bulk phase change temperature, Δc is the difference in the specific heat between the liquid and solid phase, $\Delta c = c_l - c_s$, where the subscripts indicate the phase, σ , the surface tension, ρ_s is the density of the metal, and κ is the mean curvature radius of the surface. Eqn (13) demonstrates a decrease of the melting temperature as the curvature at the interface increases and establishes the correlation between these two parameters as experimentally demonstrated by Kofman *et al.*⁴⁵

Font and Myers showed that using the generalised Gibbs–Thomson equation from eqn (13) one can accurately describe the melting temperature of spherical nanoparticles with radii in the 1–12 nm range. We here note that eqn (13) is multivalued and that the melting temperature for particles with a

radius below 1 nm cannot be calculated due to an inflection point on the melting curve and only the upper value can be considered physical since the lower value will give negative temperatures for a radius above 1.5 nm. In Ex-DIM the plasmon length is used to calculate the melting temperature of a particle according to eqn (13), and if the melting temperature is below the input temperature the relaxation constant is adjusted according to eqn (12).

1.2. Plasmonic spectra of nanoparticles with an inhomogeneous radial distribution of dielectric constants. Multilayered Mie model simulations

We can consider a spherical particle with a radial distribution of the dielectric constant $\epsilon(r)$ as a particle consisting of N thin (thickness Δr) spherical layers of a homogeneous material with dielectric constant $\Gamma_{e-ph,d}(T)$, where $r_j = j\Delta r$ is the outer radius of the j -th layer. Taking into account the spherical symmetry, multilayered Mie theory will be used to calculate the extinction spectrum.⁴⁶ The extinction cross section is in this theory defined by the following equation:

$$\sigma_{\text{ext}} = \frac{2\pi}{k^2} \sum_{n=1}^{\infty} (2n+1) \Re(a_n + b_n), \quad (14)$$

where k is the wave number, a_n , b_n are expansion coefficients of the field scattered by a particle. These coefficients can be obtained by fulfilling the boundary conditions for each inter-layer boundary:

For the outer border:

$$\begin{aligned} a_n m_N \xi'_n(x_N) - m_N \psi'_n(x_N) + d_n^N \psi'_n(m_N x_N) - g_n^N \chi'_n(m_N x_N) &= 0 \\ a_n \xi_n(x_N) - \psi_n(x_N) + d_n^N \psi_n(m_N x_N) - g_n^N \chi_n(m_N x_N) &= 0 \\ b_n m_N \xi'_n(x_N) - m_N \psi'_n(x_N) + c_n^N \psi'_n(m_N x_N) - f_n^N \chi'_n(m_N x_N) &= 0 \\ b_n \xi_n(x_N) - \psi_n(x_N) + c_n^N \psi_n(m_N x_N) - f_n^N \chi_n(m_N x_N) &= 0. \end{aligned} \quad (16)$$

In addition, from the condition of finiteness of the field amplitudes in the nanoparticle center we find $f_n^1 = g_n^1 = 0$. Here c_n^j , d_n^j , f_n^j , g_n^j are expansion coefficients of the field in the j -th layer, $m_j = \sqrt{\epsilon_j}$ is the refractive index of the j -th layer, $x_j = kr_j$ is the outer radius of the j -th layer (in wavelength unit), $\psi_n(z) = z j_n(z)$, $\chi_n(z) = -zy_n(z)$, $\xi_n(z) = z h_n^{(1)}(z)$ are the Ricatti-Bessel functions, and symbol ($'$) denotes a derivative.

To obtain the radial dependence of the dielectric constants in a particle we use the Drude model as described in ref. 26.

$$\epsilon(r, \omega) = \epsilon_0(\omega) - \frac{\omega_p^2}{\omega^2 + i\omega\Gamma}, \quad (17)$$

where ω is the cyclic frequency of the electromagnetic field, $\epsilon_0(\omega)$ is the component of the dielectric constant

corresponding to contribution of the interband transitions which is fitted by means of experimental data⁴⁷ that makes it possible to accurately reproduce these experimental data in the framework of the Drude model, ω_p is the plasma frequency, Γ is the size dependent relaxation constant.

$$\Gamma = \Gamma_0 + A_r \frac{v_f}{R}. \quad (18)$$

Here v_f is the Fermi velocity, R is the particle radius, A_r is the constant assumed to be equal to 1, Γ_0 is the size-independent component of the relaxation constant for bulk metals. In these materials the mobility of atoms is close to that in the nanoparticle core because it does not experience the influence of the surface layers, being deep in the center of the particle.

To obtain this dependence, we use the dependence of the relaxation constant on the temperature for a bulk:

$$\Gamma_0(T) = \begin{cases} A_0 T_e + B_0, & T_e < T_m \\ 2.4(A_0 T_m + B_0), & T_e > T_m. \end{cases} \quad (19)$$

Here T_m is the melting temperature, A_0 and B_0 are linear coefficients determined in.²⁶ In this approach, instead of the particle temperature, we use the effective temperature T_e that corresponds to the temperature in bulk with the same mobility of atoms (δ) in the particle, as well as in the particle layer (see the definition of δ in section 1.3.3).

We can obtain the dependence $T_e(\delta)$ (in particular, for $r = 0$ as the point closest to the conditions of a bulk) from the results received by molecular dynamics methods (see section 1.3) using approximation for different temperatures. Similarly, the radial dependence $\delta(r)$ can be obtained by approximating the calculated data on the mobility of atoms at a fixed temperature. We note here that the extinction cross section of the plasmonic nanoparticles studied in our work is close to the absorption cross section, since the contribution of scattering at such small sizes is negligible.

1.3. Molecular dynamics and mobility simulations

1.3.1. Embedded Atom Model Molecular Dynamics simulations. We have performed MD calculations of spherical gold nanoparticles to explore their behavior as a function of the simulation temperature and to obtain a detailed observation of the motion of atoms and of the vibrational properties of different parts of the nanoparticles. These simulations were performed using the Embedded Atom Model (EAM)⁴⁸ potential implemented in the LAMMPS code.^{49,50} The EAM potentials were initially developed to represent the metallic bonding behavior and therefore are known to provide an accurate description of mechanical, kinetic and even vibrational properties of gold.⁵¹ In this study we have chosen the parametrization by Foiles *et al.*⁵² because it is capable of representing temperature-dependent elastic properties of Au.⁵³ For higher accuracy of the atomic trajectory calculations, the MD time step was set to 0.5 fs in all calculations. The temperature was controlled by

a Nose-Hoover thermostat⁵⁴ with the temperature damping parameter of 50 fs.

An NP was cut out of bulk FCC/fcc gold crystal as a sphere with a diameter of 6 nm and containing 6531 atoms. At that size of nanoparticle only slight discrepancies from the ideal spherical shape are observed as small (111) facets. The NP was pre-annealed at the temperature 700 K for 100 ps with subsequent cooling down to 300 K in another 100 ps. During annealing only single events of atom migration from vertices and edges to the facets are observed. Therefore, the shape of the NPs does not change significantly and remains almost spherical. After that, the temperature was being increased at a rate of 0.1 K ps⁻¹ up to 1200 K and at every 50 K the atomic motion was recorded.

The dynamics of atoms at each temperature was registered with 10 000 consecutive configurations taken every 1 fs. A preliminary analysis of all the MD trajectories confirmed the stability of the structure, which preserved crystallinity and morphology till 900 K.

1.3.2. ReaxFF molecular dynamics simulations. A reactive force field model was also used for temperature dependent molecular dynamics simulations focusing on particle behaviour at very high temperatures beyond melting. The initial configurations were first energy minimized through low-temperature (10 K) molecular dynamics (MD) simulations in the canonical ensemble (NVT) for about ten picoseconds. Then, the temperature was slowly increased from 10 to 293 K (in a period of about 15 ps), and equilibration at that temperature was carried out for about 100 ps. The simulations were further extended for production (50 ps), and the last 100 sampled structures were extracted and used for the subsequent calculations. Au NP configurations were collected every 0.01 ps. To explore the behavior of the Au NPs as a function of the simulation temperature series of progressive NVT MDs, namely a slow temperature increase (12 ps), equilibration (150 ps), and production (100 ps), were carried out. The last 100 configurations sampled every 0.01 ps were selected for the subsequent calculations. All the MD simulations were based on an earlier parametrized reactive force field.⁵⁵⁻⁵⁷

A preliminary analysis of all the MD trajectories confirmed the stability of the structures, which preserved both their morphology and crystallinity till 950 K, having almost unchanged low index faces and no visible adatoms. The ReaxFF MD simulations were carried out by means of the Amsterdam Density Functional (ADF)/ReaxFF code.⁵⁸ The simulation temperature was controlled through Berendsens thermostat with relaxation constants of 0.1 ps, and the time step was set to 0.2 fs.

1.3.3. Characterization of the atom mobility and its definition. To control transformations of the internal structure of the Au particles we used several parameters, *e.g.* the lattice parameter for the first coordination sphere and the standard deviation of atomic coordinates from the averaged value for the $N_{ts} = 100$ last time-steps in the molecular dynamics simulations.

Let r_{ij}^m be the distance between the centers of the i -th and j -th atoms at the m -th time step and η_i^m is the set of the atom

indices (number) that are located in the first coordination sphere at the m -th time step (N_{ts} is the number of steps). The lattice parameter L for the i -th particle corresponds to the mathematical expectation (R_i^m) of the distance to the neighboring atom in the first coordination sphere

$$R_i^m = \frac{1}{|n_i^m|} \sum_{j \in n_i^m} r_{ij}^m \quad (20)$$

$$L_i = \frac{\sqrt{2}}{N_{ts}} \sum_{m=1}^{N_{ts}} R_i^m,$$

here the multiplier $\sqrt{2}$ takes into account the FCC lattice feature which relates the lattice parameter to the distances between the atoms in the first coordination sphere. The standard deviation of the atom coordinates from the averaged value within the entire particle is calculated as

$$\delta_i = \frac{1}{N_{ts}} \sqrt{\sum_{m=1}^{N_{ts}} (r_i^m - r_i^{av})^2}, \quad (21)$$

$$r_i^{av} = \frac{1}{N_{ts}} \sum_{m=1}^{N_{ts}} r_i^m. \quad (22)$$

Here r_i^m is the coordinate of the i -th atom at the m -th time step. The coefficient δ_i corresponds to the temperature dependent mobility of the atoms growing to the melting point.

We note that a similar definition in paper⁵⁹ of the mobility of atoms in a crystal lattice in paper⁵⁹ also used the mean square relative atomic displacement dependent on temperature and pressure.

2. Results and discussion

2.1. Structural evolution of Au nanoparticles upon heating

We analyze first the temperature dependence of the mobility in the center of a 6 nm Au nanoparticle, see results presented in Fig. 1. The choice of the mobility measurement point is motivated by that the conditions for the surrounding atoms in

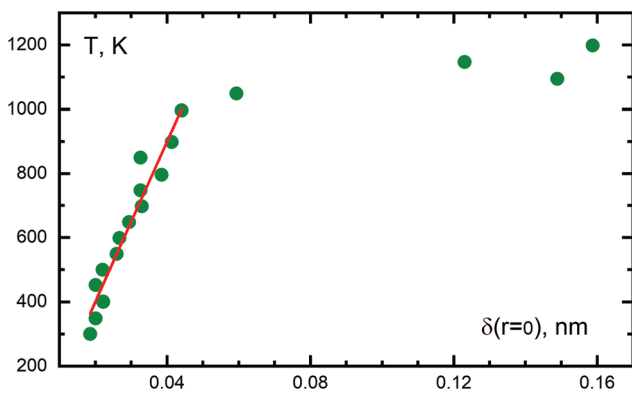


Fig. 1 The temperature dependence of the mobility of atoms in the center of a 6 nm Au nanoparticle with a linear approximation below the melting point. The EAM molecular dynamics simulations.

this location as well as the crystal lattice structure are similar to that in bulk and are not affected by the boundary of the particle. As we can see from this figure, a slow monotonic increase in this parameter is replaced by a sharp jump close to the melting point in the temperature range from 1000 K to 1050 K and above, at which point a phase transition occurs. The latter corresponds to the onset of an amorphous structure formation when the melting point is reached. When the temperature continues growing, the mobility demonstrates a slow monotonic growth, which may be accompanied by evaporation or even fragmentation of the particle at extremely high temperatures as shown in Fig. 2. Note that the simulation of melting shown in this Fig. 2 gives only a qualitative view of the process of particle evolution as the temperature increases. This particle behavior is typical for the conditions of instantaneous heating, for example, by a picosecond laser pulse, when the thermodynamic state of the particle is not in equilibrium with the thermostat. Such laser-induced fragmentation of metal nanoparticles has been experimentally observed, see in particular ref. 60.

Calculated data available in the literature on the size dependence of the melting temperature of free particles have a wide dispersion of values. These data depend on the employed model, as well as on the initial shape of the particle (*e.g.* round or faceted Wulff-constructions). The papers by Sclexer⁶¹ and Guisbiers⁶² present comparative results from applications of the effective medium theory (EMT) and the embedded atom model (EAM), as in our case. The calculated value of T_m obtained with EAM for a 6 nm nanoparticle is close to our data. That paper also presents experimental data on the melting temperature for Au particles with size $D \leq 5$ nm which demonstrate very large dispersion ΔT_m (over 200 K).

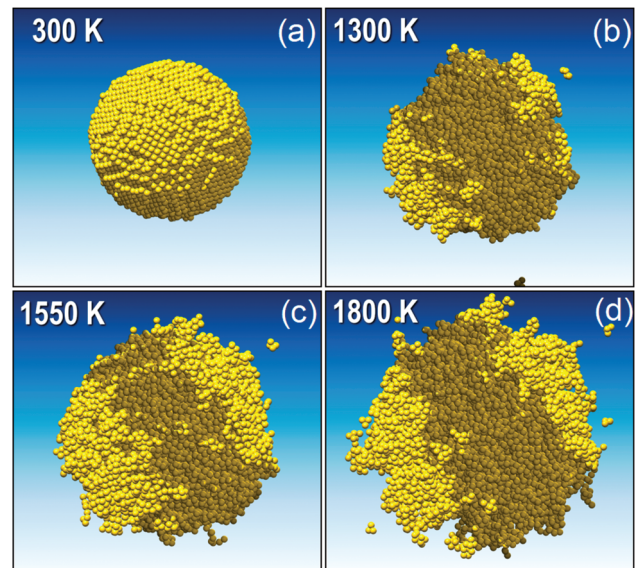


Fig. 2 Reactive force field model simulation of the evolution of the Au nanoparticle shape upon temperature growth – from the initial state at room temperature ($D = 6$ nm) directly to extremely high temperature values much above the melting point.

Experimental data in different papers have been obtained either for particles in a matrix or on a substrate. A noticeable effect of substrates on the melting temperature has been pointed out, namely that the melting temperature always then increases compared to free particles and becomes more pronounced with increasing conductivity of the substrate. In papers^{63,64} the substrate effect on the melting temperature was investigated for gold nanoparticles, showing that a high conductivity of the substrate material increases the melting temperature. The size effect on the melting temperature of gold particles was studied experimentally by Buffat and Borel⁶⁵ in one of the first papers on this subject. Their experiment with Au nanoparticles was carried out on a carbon film substrate that gives $T_m = 1100$ K for a 6 nm Au nanoparticle.

Fig. 3(I) shows the radial dependence of mobility in the 6 nm Au particle at different temperatures. Determination of this parameter makes it possible to calculate not only the averaged value over the entire volume of a particle, but also the values in the selected parts or spherical layers in a particle. Fig. 3(I and II) demonstrates some interesting physical features, first of all, the pronounced radial dependence of the mobility. It shows that the mobility near the particle surface is much higher than in its core, which means that melting starts from the surface of the particles and progresses gradually towards the inner layers during the heating. It is also clear that the melting of the surface layers occurs at lower temperatures than in the core. This feature is visually evident in the sectional view of particles at different temperatures (especially at $T = 1000$ K) revealing the structure, amplitude and state of mobility of the atoms. These images reproduce the degree of disorder increasing upon the temperature growth and detected by the TEM analysis at high resolution for different temperatures.⁶¹ An available experimental evidence of this process is confirmed by the phenomenon of fusion of contacting metallic nanoparticles, combined into a dumbbell with formation of a bridge between them during heating at temperatures well below the melting temperature of single particles, see *e.g.*^{66,67}

The spatial dispersion of the mobility of atoms $\delta_i(r)$ can here be explained by the presence of the different parts inside the particle with different lattice parameters and by the decrease of binding energy of atoms in the lattice closer to the particle boundary. In general, the atomic mobility parameter is related to the specific electrical conductivity of a metal due to the electron–phonon scattering, which is responsible for the growing of the electron relaxation constant of a metal and the suppression of the surface plasmon resonances of the nanoparticles. We explain this as follows: first, the random thermal vibrations of atoms in the lattice and the amplitudes of phonons are temperature dependent parameters which can be obtained by the Fourier transform of the time dependent function of the modulus of the i -th atom coordinate in the particle ($|\mathbf{r}_i(t)|$) at different temperatures $\rho_\omega = (1/\sqrt{2\pi}) \int_0^{t_0} r_i(t) \exp(-i\omega t) dt$. Fig. 3(III) demonstrates the spectral density of phonon modes or the total over the unit frequency range ($\Delta\omega = 1$ Hz) vibration amplitude (ρ_ω) as a function of frequency ω corresponding to different temperatures.

These Fourier spectra were averaged over all atoms of the particle. The time interval during which the function $|\mathbf{r}_i(t)|$ is recorded was equal to $t_0 = 10$ ps in the frequency range up to 10^{12} Hz. The spectra demonstrate thermal fluctuations of atoms in the crystal lattice. As we can see the spectral density of the phonon amplitudes (falling in a unit spectral range) at the frequency of 10^{11} Hz and below increases by 20 times and higher from the room temperature to the melting point.

Determination of the relationship between the amplitude of thermal vibrations of the crystal lattice of metals, electron–phonon scattering and the electron relaxation constant is an important issue in plasmonics, just as it is in condensed matter physics in general. Experimentally, the thermal vibrations of the crystal lattice and the state of the phonon spectrum can be detected by scattering of X-rays or neutrons when they pass through a sample. Such scattering is described by the Debye–Waller factor (W) and corresponds to the exponential attenuation of the transmitted flow ($I = I_0 \exp(-W)$). The dimensionless parameter W is proportional to the mean square of the vibration amplitude, which, in turn, for the case of high temperatures ($T \gg T_D$), is proportional to the absolute temperature, where T_D is the Debye temperature.

The relaxation processes limiting the conductivity of metals is known to be related to the free path of conduction electrons $l = v_\tau \tau$, where τ is a mean free run time, $v_\tau \sim \sqrt{k_B T/m_e}$ is the average velocity of the thermal motion of the electrons. In the general case the electrical conductivity coefficient (at the electron concentration n) is determined as $\sigma_0 = e^2 n l / (m_e v_\tau)$.

According to the Matthiessen rule, the dominant factor in the decrease of conductivity of pure metals with a defect-free crystal lattice is the scattering of conduction electrons by phonons, which increases in proportion to the first power of temperature at its high values, ranging from the Debye temperature up to the melting point.⁶⁸ The electron–electron component of electrical resistivity is observed only at low temperatures (well below 300 K).^{68,69} The scattering of electrons on the surface of the particle is taken into account in eqn (18) for quantum-size effects that does not depend on temperature.

In general, phonon vibrations cover a wide frequency range. The free path of an electron (l_{ep}) due to its interaction with the lattice depends on the phonon frequency, which in turn is limited from above by the condition $\omega \leq \omega_0$, where $\omega_0 = v_s L^{-1}$, v_s is the speed of sound in a metal (3200 ms^{-1} for a gold). Under the condition $T \gg T_D$ the mean free path is $l_{ep} \sim \hbar_\tau(k_B T)$. In this case, the specific resistance due to the phonon contribution corresponds to the equation

$$\rho_{ph} = \frac{m_e v_\tau}{e^2 n l_{ep}} \quad (23)$$

It is also notable that when approaching the melting temperature, the concentration of defects such as vacancies in the crystal lattice of a particle increases. The effect can be described by the additional term ($\rho_d = m_e v_\tau / (e^2 n l_{epd})$) when the free path of electrons (l_{epd}) is reduced. In this case, the specific resistance accumulates both factors $\rho = \rho_{ph} + \rho_d$ that will also cause an increase in the electron relaxation constant in a wide

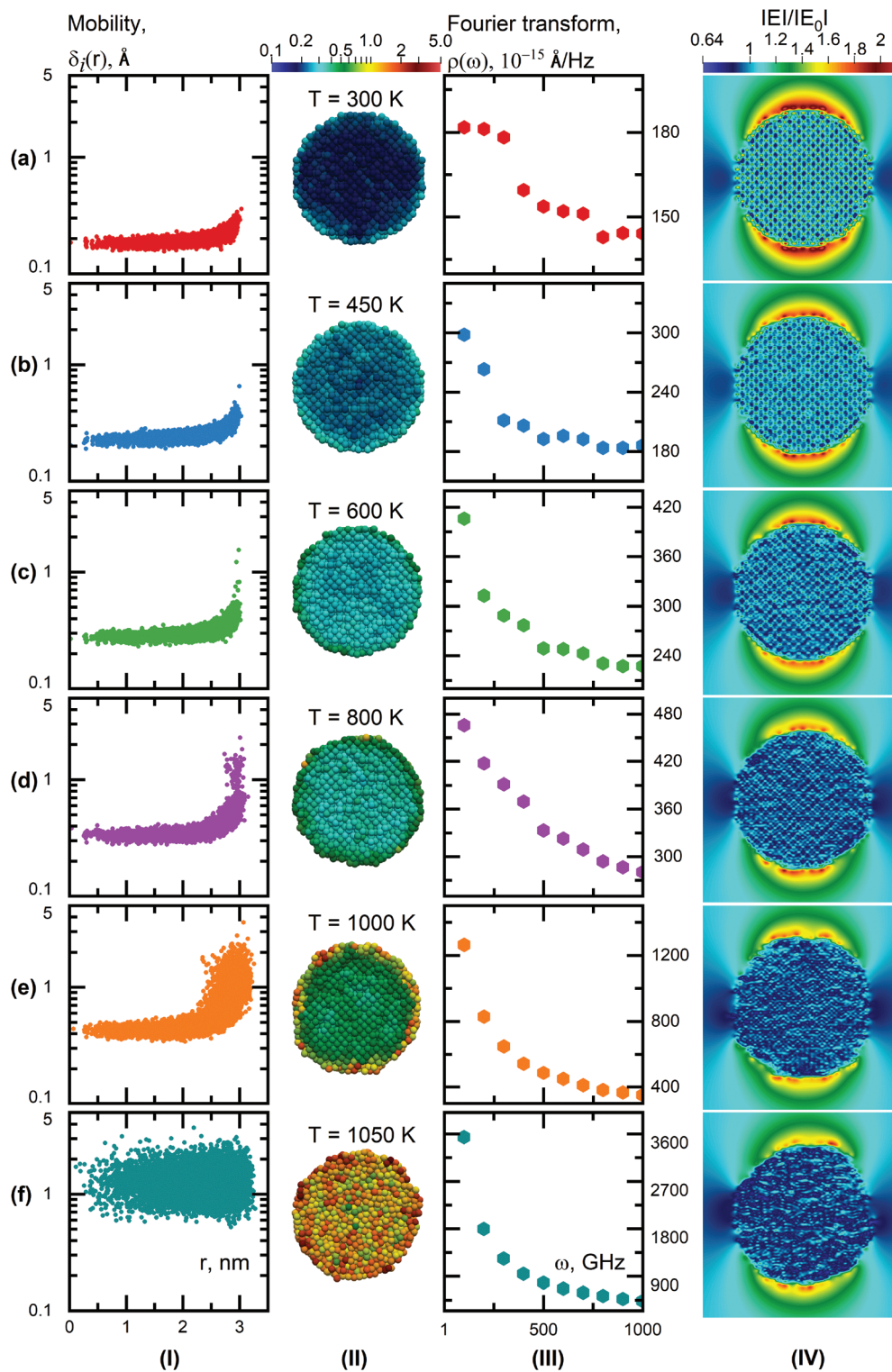


Fig. 3 Temperature dependencies (columns I, II, III, IV) of the atomic mobility in an Au nanoparticle with radius $R = 3$ nm (I), view of this mobility in the particle cross-section with internal structure (II), the Fourier transform of the time dependent modulus of the i -th atom coordinate ($|r_i(t)|$) as a spectral density of states in a unit range $\Delta\omega_i$ within in the frequency range up to 10^{12} Hz (III), and distribution of the local field inside the particle and near its surface with raising temperature (for vertical polarization) (IV).

frequency range. The specific resistance is proportional to the temperature of the metal which, in turn, is proportional to the mean square of the amplitude of phonon vibrations $T \propto \langle |\mathbf{r}_{0i}(t)| \rangle^2$. Thus, this reasoning indirectly explains the increase in the specific resistance upon the temperature growth and hence in the electron relaxation constant of a particle as well, as shown in Fig. 3(III).

2.2. Evolution of Au nanoparticle extinction spectra during heating

It is pertinent to put our new data into context of literature findings: in our earlier papers^{27–29,70} we studied the influence of pulsed laser radiation on plasmonic Ag nanoparticle aggregates and took into account the effect of melting of the nanoparticles on their resonance properties^{29,70}. This factor is accompanied by an unusual feature – a cyclically repeating rise and fall of the temperature of the resonantly excited nanoparticles within a nanosecond laser pulse. The cycles occur due to the ceasing of resonant interaction of radiation with liquefied particles having a suppressed surface plasmon resonance and the following recovery of the surface plasmon resonance during cooling and subsequent reheating. In papers^{26,29} we took into account the heating factor of plasmonic nanoparticles and their aggregates at a temperature above the melting point during interaction with pulsed laser radiation, which is accompanied by a suppression of the resonant properties of the liquefied plasmonic nanoparticles. Thereby we showed that the results obtained with and without taking into account the melting factor differ dramatically. However, in that study any experimental evidence of suppression of surface plasmon resonance was not available, and only calculated data were used based on the spectral dependencies of the dielectric constants of the metal at temperatures above and below the melting point.

The features of melting of metal nanoparticles and associated processes are mentioned in a number of papers, in particular, in refs. 30,71,72 including the heating of plasmonic nanoparticles due to interaction with radiation and peculiarities of the nanoparticle layer-by-layer melting at high temperatures,^{60,73} and measuring the optical constants for gold in thin films⁷⁴ necessary for simulations of melting. The model presented in paper⁴⁵ makes it possible to estimate the thickness of a liquid layer of a metal around the solid core of a nanoparticle with a given nanoparticle size at different temperatures and the kinetics of the melting process. In papers^{26,75,76} we presented the effect of temperature on the resonance properties of plasmonic nanoparticles within a wide range of variation of this parameter, both experimentally and theoretically. This effect underlies the dynamic photochromic effects in multiparticle plasmonic aggregates observed using picosecond laser pulses.^{70,77,78} In the latter case we accounted for the available data on the temperature dependence of the optical constants of the material.

2.2.1. Multilayered Mie model simulations of plasmonic excitations. The spectral dependences of dielectric constants on temperature approximated by continuous functions based

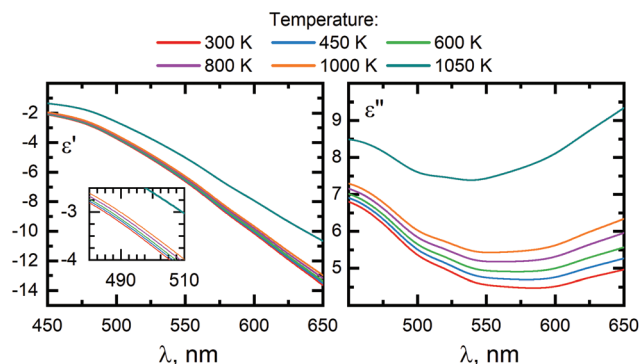


Fig. 4 Spectra of dielectric constants (real “left” and imaginary “right” parts) for gold adapted to the experimental data by Otter⁴⁷ vs. temperature. Insets show enlarged fragments of the sets of curves for the real part in a narrow spectral range.

on a discrete set of experimental data for Au bulk by Otter⁴⁷ are shown in Fig. 4. As can be seen in this figure, the main reason for the suppression of the surface plasmon resonance with growing temperature is the increase in the imaginary part of the dielectric constants, which is responsible for the radiation energy loss in the particle, and related to the electron-phonon scattering. Employing the temperature dependence of dielectric constants, one can obtain the dependence of the mobility on the dielectric constants by comparison with the temperature dependence of the mobility, see Fig. 1. Having obtained data on the radial distribution of the dielectric constants in the nanoparticle for each temperature value, one can perform calculations of the extinction of such a plasmonic particle using Mie theory applied to the core-shell model.⁴⁶ Note, that for each particle radius the size correction to the dielectric constants should be taken into account.

Fig. 5(a and b) shows the evolution of the extinction spectra of an Au nanoparticle for each temperature value with the surface plasmon resonance at the wavelength $\lambda = 490$ nm in vacuum. For comparison, two models were used in these calculations: (a) taking into account the inhomogeneous distribution of the dielectric constant along the radius, and (b) using a simplified approach with a homogeneous distribution of the dielectric constant throughout the particle volume, which we employed earlier. To determine the radial dependence of the dielectric constants inside the particle we used the temperature dependence of the mobility of atoms in the particle in Fig. 1, as well as the radial dependence of the mobility at different temperatures in Fig. 3(I), shown as a set of statistically scattered points. This dependence was represented by the approximation curve $T(\delta)$, in which the temperature scale was correlated with the dielectric constant $\epsilon(T)$ (see Fig. 4).

The series of spectral curves demonstrates a stable tendency towards the suppression of the plasmon resonance with increasing temperature. In the range of moderate temperatures, the rate of decrease in the amplitude is rather slow, similar to the results in paper.⁷⁹ When approaching the point

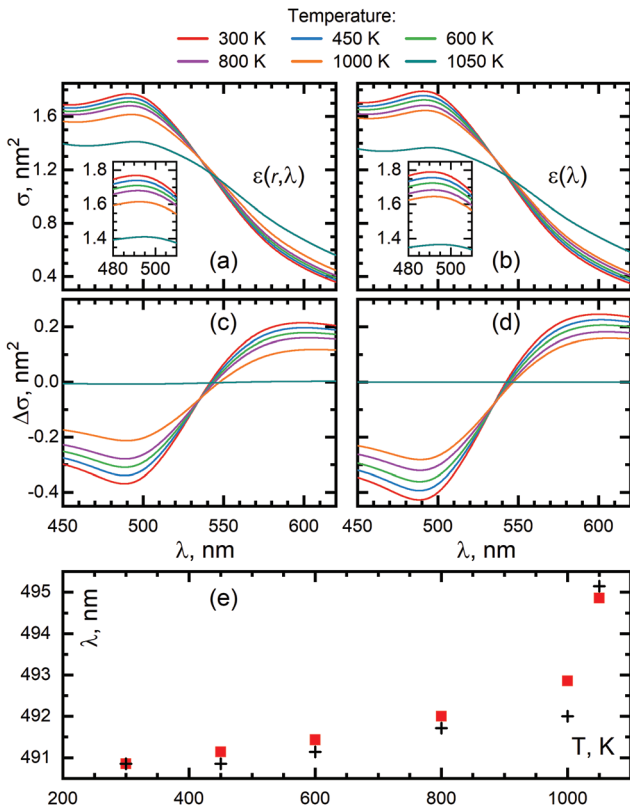


Fig. 5 Variation of the extinction spectra and differential extinction spectra of a 6 nm Au nanoparticle in vacuum and suppression of surface plasmon resonance in the temperature range 300–1200 K with a radial dependence of the dielectric constant (a, c), and in the absence of radial dependence of dielectric constant (b, d) in a vacuum (refractive index $n_0 = 1$). Shift of the wavelength corresponding to the maximum in the extinction spectra of a 6 nm Au nanoparticle upon the temperature growth (e): for the inhomogeneous (square dots) and the homogeneous (crosses) radial dependencies of the dielectric constant.

of the phase transition, a abrupt drop of the plasmon resonance amplitude is observed. Note, approaching a temperature of the melting point and above it, the optical properties of the plasmonic nanoparticles are determined not only by the thermal variation of the dielectric constants, but also by the dynamical chaotization of the particle shape, which is accompanied by a broadening of the plasmonic spectrum and emergence of additional resonances for each instantly existing shape.^{80,81}

Differential spectra of the Au nanoparticle extinction and the difference in spectra based on different models are shown in Fig. 5(c and d). As can be seen from this figure, there is a general tendency for the plasmon resonance to become suppressed with growing temperature. However, taking into account the inhomogeneity in the radial distribution of the dielectric constant results in a higher rate of suppression with growing temperature compared to the case of a homogeneous dielectric constant distribution. This is explained by the fact that at the same temperature and dielectric constant at the center of the particle, the first model takes into account the

change in the dielectric constant in the spherical layers close to the surface, first of all, an increase in its imaginary part, which is accompanied by an accelerated suppression of the resonance. Fig. 5(e) shows that besides the decrease of the plasmon resonance maximum, a long-wavelength shift of the resonance is observed with raising temperature. Here the spectra taking into account the radial dependence of the dielectric constant in the nanoparticle demonstrates a more pronounced effect, similar to the experimental result, compared to the case of the homogeneous distribution.

2.2.2. Ex-DIM simulations of plasmonic excitations. Fig. 3 (II and III), demonstrates the chaotization of the crystal lattice structure, the increase of vibrational amplitude and growing mobility of atoms seen in a sectional view of the particle occurring at raising temperatures. The question arises how the chaotization of the Au nanoparticle crystal lattice with growing temperature affects the plasmonic spectra? Here, the unique capabilities of the Ex-DIM make it possible to account for the effect of the crystal lattice geometry of a nanoparticle in its pure form on the plasmon absorption spectra. In our case, the geometry change involves an increase in the crystal lattice constant as well as a randomization of the lattice with growing temperature. Fig. 6(a and b) demonstrates the structural effect on the extinction spectrum shown at different temperatures. In these simulations the relaxation constant was maintained unchanged and corresponds to the room temperature of 300 K. As follows from the figure the structural effect on the spectrum from single snapshots at different temperatures is negligibly small. To show that this is no coincidence a statisti-

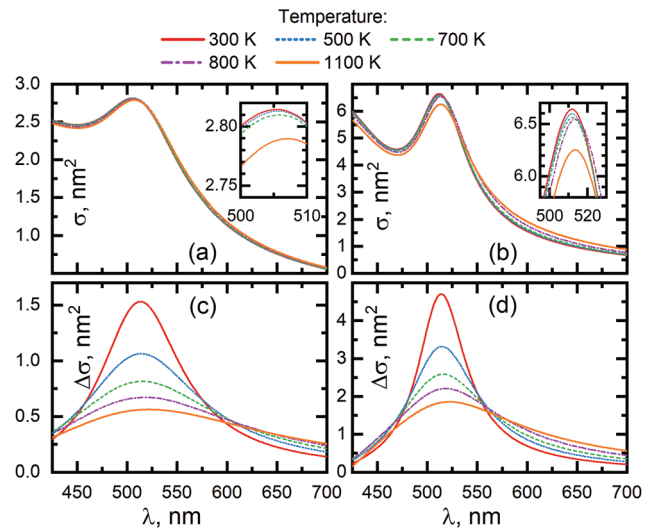


Fig. 6 Ex-DIM simulations of the structure effect on the extinction spectra for the 6 nm Au nanoparticle. Geometries are taken at different temperatures but with relaxation constant fixed at the room temperature $\Gamma_r(T = 300 \text{ K})$. Insets show the enlarged fragments of spectral curves near the surface plasmon resonance maximum to highlight minor differences in the curves. Plasmonic absorption spectra of the 6 nm Au nanoparticle with subtracted interband absorption band of gold at different temperatures. (a, c) – in a vacuum ($n_0 = 1$), (b, d) – in a medium with a refractive index of $n_0 = 1.33$.

Table 1 Statistically averaged structural effects on maximum of the surface plasmon resonance (λ) and extinction cross section σ_{ext} along with the standard deviation $\sigma(\lambda)$ and $\sigma(\sigma_{\text{ext}})$ for both properties. T shows the temperature for the snapshot, all calculations have been performed at 300 K in the Ex-DIM. NPs in the top section are in vacuum while the middle section corresponds to the ambient medium with the refractive index of $n = 1.33$. In the last line the snapshots and temperature in the Ex-DIM is 500 K. These calculations have been performed for particles in a medium with the refractive index of $n = 1.33$

T [K]	λ [nm]	$\sigma(\lambda)$ [nm]	σ_{ext} [nm ²]	$\sigma(\sigma_{\text{ext}})$ [nm ²]
300	505.4	0.1	2.814	0.004
500	505.59	0.03	2.813	0.001
700	505.87	0.08	2.811	0.002
900	507.0	0.1	2.817	0.003
1100	507.5	0.3	2.804	0.009
300	511.8	0.2	6.64	0.02
500	511.8	0.2	6.603	0.008
700	512.2	0.1	6.56	0.01
900	513.6	0.2	6.56	0.02
1100	513.7	0.3	6.31	0.05
500	508.0	0.1	5.290	0.005

cal analysis of 100 randomly selected snapshots at each temperature was performed, see Table 1. It demonstrates that the red shift in the surface plasmon resonance from the structural effects remains within 2 wave numbers and that the decrease in the extinction cross section in vacuum is only 0.4% while in the medium with the large refractive index the decrease is 5%. The variations between the snapshots at a given temperature is even smaller as seen from the standard deviation of both the surface plasmon resonance and extinction cross section.

A similar statistical analysis from raising the temperature in the Ex-DIM unfortunately gives difficulties in pinpointing the maximum of the surface plasmon resonance because of the absence of a definite peak at higher temperatures. It is, however, evident when comparing the single snapshots plotted in Fig. 6 that the structural effects almost vanish in comparison to the change from the Debye model for the phonon spectrum. In the last line of Table 1 this becomes very clear since there is a shift of almost 4 wave numbers and a decrease of 20% in the extinction cross section when comparing the Ex-DIM calculations performed at 300 K and 500 K.

Thus, an important conclusion follows from Fig. 6(a and b), namely that the randomization of the crystal lattice in its pure form, which intensifies with raising temperature, does not noticeably affect the surface plasmon resonance.

Here we see that although there is a structural dependence that suppresses the plasmon band to a small extent with temperature, the relaxation factor represents by far the most important mechanism that contributes to the temperature dependence of the suppression.

In contrast to Fig. 6(a, b, c and d) shows the extracted intraband spectral contribution of the surface plasmon resonance for the Au nanoparticles obtained by subtracting the interband absorption band at different temperatures from the total spectrum. This series of curves clearly demonstrates the suppres-

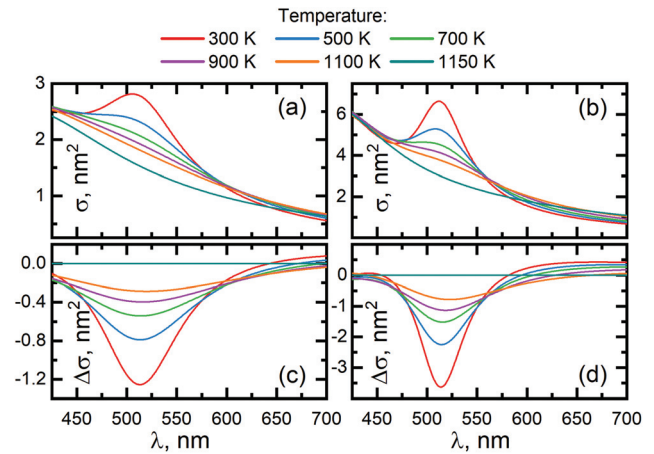


Fig. 7 Ex-DIM simulations of the extinction spectra variation for the 6 nm Au nanoparticle with suppression of surface plasmon resonance in the temperature range 300–1150 K. Differential extinction spectra variation with suppression of surface plasmon resonance in the temperature range 300–1150 K (all curves were subtracted from the spectral dependence for $T = 1150$ K). (a, b) – in vacuum, (b, d) – in the medium with refractive index $n_0 = 1.33$ (b).

sion of the surface plasmon resonance due to the relaxation processes with increasing temperature followed by melting. However, both factors are worth considering in order to interpret the overall results presented in Fig. 7.

Fig. 3(IV) demonstrates the distribution of the local field inside the particle and close to its surface with increasing temperature. The capabilities of Ex-DIM make it possible to calculate both the plasmon absorption spectra and the local field inside the particle and near its surface at the given temperature. As can be seen from the series of images, the distribution of the local field inside the heated particle and near its surface is inhomogeneous. The maximum values of the field strength inside the particle and near its poles are achieved at minimum temperatures and in conditions of the ordered crystal lattice. The pattern of the local field distribution near the particle surface corresponds to the classical one for a spherical geometry. However, with raising temperature, the field strength near the poles decreases and deviates from the classic configuration, which is associated with the growing contribution of the relaxation processes, suppressing the plasmon oscillations. It is also notable that overall decrease in the amplitude of the internal local fields inside the particle as the temperature rises and when the crystal structure amorphizes. Attention is drawn to the perturbation of the field near the particle surface, associated with deviations of the particle shape from the sphere at high temperatures.

Fig. 7 clearly demonstrates the suppression of the surface plasmon resonance with increasing temperatures. Due to the rapid suppression of resonance in the range from 300 K to 700 K it becomes difficult to visibly distinguish the surface plasmon resonance above 700–900 K without comparing with the spectra at 1150 K where the particle is melted. We here note that the melting temperature in the Ex-DIM calculated from the Gibbs–Thomson equation – eqn (13) is 1130 K.

The suppression of the surface plasmon resonance, as calculated by Ex-DIM, is predicted to be faster at lower temperatures than from the multilayered Mie theory, as seen in Fig. 7, where a more linear correlation between the maximum value of the surface plasmon resonance and temperature is observed. For the maximum of surface plasmon resonance, there is a wavelength difference of less than 10 nm between Ex-DIM and the multilayered Mie theory. This difference is primarily due to the size correction for the multilayered Mie theory for the case of gold²⁶ and the discrete nature of Ex-DIM, where the number of atoms in a particle with the same radius can vary and hence give a small change in the position of the surface plasmon resonance. The calculations of the plasmonic spectra of Au nanoparticles performed for different values of the refractive index of the environment coincide with the trend shown by K. G. Thomas.⁸²

In order to better observe the temperature suppression of the surface plasmon resonance, the differential spectra between the solid and melted (1150 K) nanoparticles are plotted in Fig. 7(c and d). Here the contribution from the surface plasmon resonance at different temperatures becomes more visible along with the slight red shift of the resonance as temperature grows.

2.2.3. Comparison with experiment. Fig. 8 shows a comparison between available experimental data and the results of calculating the extinction spectra with raising temperature. The slope of these dependencies corresponds to the rate of suppression of the surface plasmon resonance. The range of variation of the extinction cross section values is expressed through the difference of the maximum to the minimum value in the investigated temperature range comprising the room temperature and the melting point. Since we compare the temperature dependence of the surface plasmon resonance amplitude of different size particles – 6 nm in calculations and 40 nm in our experiments Fig. 8, we limit ourselves to a comparison of the general trends in the spectra. We note that an exact comparison with experiment cannot be made due to the

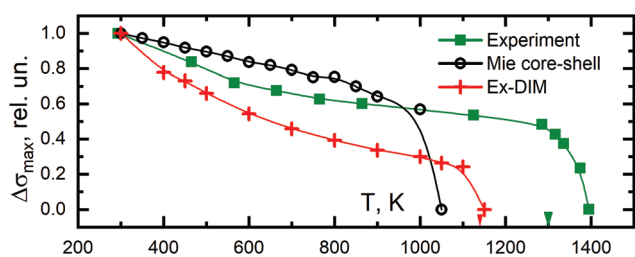


Fig. 8 Comparison of the suppression rate for the maximum of plasmonic spectrum upon the temperature growth calculated by the multilayered Mie theory in the case of inhomogeneous radial dependences of the dielectric constant in a 6 nm Au nanoparticle (circles), by Ex-DIM with homogeneous radial dependences of dielectric constant (cross dots) – both in vacuum ($n_0 = 1$), and in experimental extinction spectrum of a 40 nm Au nanoparticles on quartz substrate (square dots).⁷⁵ Arrows on the temperature scale show the melting points for the 6 nm and 40 nm nanoparticles.

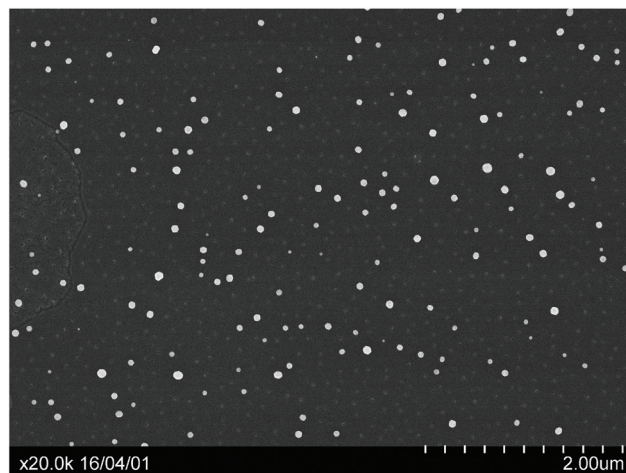


Fig. 9 SEM image of Au nanoparticles on quartz substrate after annealing. The mean size of the nanoparticles is 40 nm.

size dependent melting temperatures (T_m) – for the 6 nm Au nanoparticle the melting point is obtained from the Gibbs–Thomson equation as 1130 K, whereas for the 40 nm nanoparticle the melting is observed at 1300 K (both values are marked on the temperature axis of this figure).

As can be seen from Fig. 8 the calculated and experimental dependencies with the thermal suppression rate of the surface plasmon resonance amplitude are generally similar. Calculations of the extinction spectra were carried out by two methods: Ex-DIM and the multilayered Mie theory. In both cases there is a slow and monotonic decrease in the amplitude with raising temperature, and when the melting temperature is reached an abrupt drop in the resonance amplitude occurs that qualitatively reproduces the experimental result. It is notable that the shape of the curves in Fig. 8 when comparing the calculated and experimental data can also be an indicator of their similarity besides a sharp drop when approaching the melting point. However, this is a subject of separate studies.

Fig. 9 shows SEM images of Au nanoparticles on a quartz substrate subject to heating up to the melting point and above in our experiment. The average size of polydisperse Au particles is here about 40 nm.

3. Conclusions

The intriguing issues related to melting of small metal nanoparticles induced by strong laser fields, and the altered behaviour of plasmonic excitations with temperature, form interesting subjects for fundamental studies, but finds also motivation in the large number and a variety of applications of plasmonic nanoparticle technology. These considerations led us to initiate the present work, where we studied the behaviour of plasmon resonances of metal nanoparticles as the temperature goes from room conditions to the melting point. This was accomplished by engaging the Extended Discrete Interaction

Model (Ex-DIM) for predicting plasmonic excitations where the basic structural data for the nanoparticles were obtained by means of molecular dynamics simulations. A semi-empirical theory for relaxation constants of the plasmonic excitation states was thereby also employed, as well as a classical approach based on the multilayered Mie theory. As a prerequisite to studying the plasmonic spectral dependency on temperature we also computationally explored the actual melting process, and the dependence of the atom mobility in the crystal lattices with heat.

We find that heating of plasmonic nanoparticles, including super-high heating, changes not only the dielectric constant due to the electron–phonon scattering, but the size and shape of particles as well. In the liquid state the shape can dynamically vary from spherical to chaotic as shown in Fig. 2. Even at room temperature complex-shaped particles, unlike spherical ones, acquire additional resonances in the plasmonic absorption band, which is accompanied by a broadening of this spectral band.⁸¹ At the same time, in real conditions of picosecond laser heating of nanoparticles both features – change in the shape and structure and change in the dielectric constant – will manifest themselves jointly. In particular, these factors may serve as additional sources of optical nonlinearity of a nanocomposite medium containing plasmonic nanoparticles.

Based on the obtained results in this work, we can make the following statements:

1. The mobility of atoms in the crystal lattice of heated nanoparticles clearly demonstrates staged features when the temperature approaches the melting point. Upon temperature growth this mobility first shows a slow monotonic increase which is replaced by a sharp drop close to the melting point, in which a phase transition occurs. When the temperature continues growing, the mobility demonstrates again a slow monotonic growth, leading ultimately to evaporation or even fragmentation of the particle.

2. We could predict a pronounced radial dependence of the mobility which is much higher near the particle surface than in the central part. This reflects the fact that the melting starts from the surface and progresses gradually towards the inner layers of the particle during heating. It becomes clear that the melting of the surface layers occurs at a much lower temperatures than of the core. It corroborates with the finding in the experimental paper⁴⁵ that gives evidence of the key role of the surface in melting of ultrafine particles. When approaching the melting point, the radial dependence of the mobility gradually disappears and becomes homogenized over the volume of the particle.

3. We could also show that Fourier spectra representing the average amplitude of phonon oscillations, expressed as a function of frequency, demonstrate that conditions for electron–phonon scattering arising with temperature, lead to a significant increase in the electron relaxation constant.

4. Concerning the dependence of the plasmonic spectra on temperature we could conclude that the plasmonic resonance bands slightly red shift, reproducing experimental results, and that their extinction coefficients decrease with raising tempera-

ture, becoming almost totally suppressed at the melting point.⁷⁵ The suppression of the surface plasmon resonance in the metal nanoparticle starts at temperatures well below the melting point up to full suppression after the transition of the particle into the liquid state, something that is associated with an increase in the amplitude of the atom vibrations in the crystal lattice. It is accompanied by electron–phonon scattering with simultaneous increase in the relaxation constant. The earlier melting of the surface will to a large extent dictate the dependence of the plasmon resonance on temperature.

5. The contributions of the lattice structure chaotization as well as the increase in particle size and lattice constant to the suppression of the surface plasmon resonance during heating seem quite minor. The dominant factor of suppression of the plasmonic excitation is thus the electron–phonon scattering, which significantly changes the relaxation constant.

The ramifications of these findings could be very wide and call for the optimization of the temperature conditions, and to optimize the plasmonic nanoparticles under these conditions, and concern a large number of applications that employ plasmonic nanoparticles. Thus, the particles must be optimized both to maximize the local field enhancement and to maintain maximum functionality, taking into account also the degradation of resonance properties caused by the incident radiation.

The unique combination of research tools employed in this work made it possible to look deep into processes underlying thermal effects in metallic nanoparticles, previously inaccessible for studies. These effects, often ignored in many publications cause a fundamental change in the properties of such particles during heating. The most typical conditions, under which the thermal effects occur, arise when nanoparticles are irradiated by pulsed laser radiation of high intensity. Such exposures underlie various applications related to the requirement of local field enhancement effect. The study of such processes is of topical interest for nanosensorics, plasmonically enhanced Raman scattering, nanobiomedicine and biotechnology as well as for waveguiding and near-field heat transfer

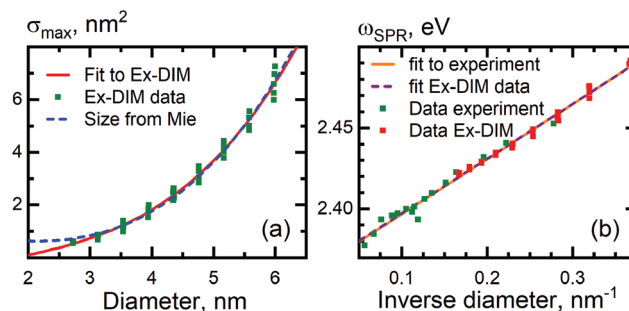


Fig. 10 Fitting the maximum value of the extinction cross section to the classical results obtained by using the parameterization of Karimi⁸⁶ (a). Fitting of the size-dependent position of the surface plasmon resonance (SPR) compared to the fit of the experimental data.^{83–85} The data points are the measured and calculated values (b). The refractive index of the host medium is here $n = 1.33$.

using plasmonic nanoparticles, all relying on the strong field and energy concentration around nanoparticles generated by plasmonic excitations.

Author contributions

All authors have equally contributed to the paper.

Conflicts of interest

There are no conflicts of interest to declare.

Appendix A: Fitting of the Ex-DIM parameters

Previously the Ex-DIM was only fitted to the position of the surface plasmon resonances from experiment and not to the absolute value of the extinction cross section.³² Since the polarizability per atom is not a constant with increasing cluster size the use of atom polarizabilities overestimates the extinction cross section.^{40,41} This means that not only are ω_a and A from eqn (6) but also the polarizability α along with the constants K_0 and K_s from the size- and temperature-dependent relaxation constants $\Gamma_{\text{size}}(P_i)$ and $\Gamma_{\text{e-ph,d}}(T)$ are to be fitted.

The positions of the surface plasmon resonances are here fitted to different experimental sources^{83–85} while the extinction cross section is fitted to Mie theory at room temperature. The parameters have been optimized by minimizing the difference between the size-dependent experimental fit and the size-dependent fit of a training set of spherical gold clusters, as seen in Fig. 10(a), along with minimizing the difference in the extinction cross section to the size-corrected Mie theory⁸⁶ as seen in Fig. 10(b). We have in this way improved the fitting procedure in comparison to the original procedure used for the Ex-DIM since the size-dependent fit is significantly closer to experiment and gives a correct absolute value for the extinction cross section. The procedure is substantially faster to perform. We find $\omega_a = 0.08735E_h$, $A_s = 2.06a_0$, $\alpha = 3.4a_0^3$, $K_s = 0.50E_h a_0$ and $K_0 = 0.005E_h$ in atomic units.

Acknowledgements

The work is supported by the Russian Science Foundation (project No. 18-13-00363). L. K. S. acknowledges the support of Carl Tryggers Stifetelse, project CTS 18-441. The authors thank the Krasnoyarsk Regional Center of Research Equipment of Federal Research Center “Krasnoyarsk Science Center SB RAS” for the use of Hitachi S-5500 high-resolution scanning electron microscope for the analysis of nanomaterials. Some of the computations were enabled by resources provided by the Swedish National Infrastructure for Computing (SNIC) at the High Performance Computing Center North (HPC2N) partially funded by the Swedish Research Council through grant agree-

ment no. SNIC 2020/3-29. Authors thank Anton Utyushev for technical assistance in preparation of Fig. 3.

References

- 1 U. Kreibig and M. Vollmer, *Optical properties of metal clusters*, Springer, 1995, pp. 13–201.
- 2 G. Shvets and I. Tsukerman, *Plasmonics and plasmonic metamaterials: Analysis and applications*, World Scientific, 2012, vol. 4.
- 3 M. I. Stockman, *Opt. Express*, 2011, **19**, 22029–22106.
- 4 V. V. Klimov, *Phys.-Usp.*, 2008, **51**, 839.
- 5 M. A. García, *J. Phys. D: Appl. Phys.*, 2011, **44**, 283001.
- 6 S. A. Maier, *Plasmonics: Fundamentals and Applications*, Springer, 2007, pp. 21–37.
- 7 B. S. Luk'yanchuk, A. E. Miroshnichenko, M. I. Tribelsky, Y. S. Kivshar and A. R. Khokhlov, *New J. Phys.*, 2012, **14**, 093022.
- 8 F. Galvez, D. P. de Lara, J. Spottorno, M. García and J. Vicent, *Sens. Actuators, B*, 2017, **243**, 806–811.
- 9 P. Cheng, Z. Ding, H. Yuan, D. Zheng, P. An, Z. Wang, H. Zhao and J. Bao, *Chem. Phys. Lett.*, 2020, **738**, 136869.
- 10 S. Ganesan, S. Maricot, J.-F. Robillard, E. Okada, M.-T. Bakouche, L. Hay and J.-P. Vilcot, *Sensors*, 2021, **21**, 2035.
- 11 L. Jauffred, A. Samadi, H. Klingberg, P. M. Bendix and L. B. Oddershede, *Chem. Rev.*, 2019, **119**, 8087–8130.
- 12 C. Chang, C. Yang, Y. Liu, P. Tao, C. Song, W. Shang, J. Wu and T. Deng, *ACS Appl. Mater. Interfaces*, 2016, **8**, 23412–23418.
- 13 A. Ershov, V. Gerasimov, A. Gavriluk, S. Karpov, V. I. Zakomirnyi, I. Rasskazov and S. Polyutov, *J. Quant. Spectrosc. Radiat. Transfer*, 2017, **191**, 1–6.
- 14 M. Lim, J. Song, S. S. Lee and B. J. Lee, *Nat. Commun.*, 2018, **9**, 9.
- 15 M. Luo, J. Dong, J. Zhao, L. Liu and M. Antezza, *Phys. Rev. B*, 2019, **99**, 9.
- 16 L. R. Hirsch, R. J. Stafford, J. Bankson, S. R. Sershen, B. Rivera, R. Price, J. D. Hazle, N. J. Halas and J. L. West, *Proc. Natl. Acad. Sci. U. S. A.*, 2003, **100**, 13549–13554.
- 17 S. Hashimoto, D. Werner and T. Uwada, *J. Photochem. Photobiol., C*, 2012, **13**, 28–54.
- 18 E. Y. Lukianova-Hleb, X. Ren, R. R. Sawant, X. Wu, V. P. Torchilin and D. O. Lapotko, *Nat. Med.*, 2014, **20**, 778.
- 19 A. Lenert, D. M. Bierman, Y. Nam, W. R. Chan, I. Celanović, M. Soljačić and E. N. Wang, *Nat. Nanotechnol.*, 2014, **9**, 126–130.
- 20 U. Guler, V. M. Shalaev and A. Boltasseva, *Mater. Today*, 2015, **18**, 227–237.
- 21 M. L. Brongersma, N. J. Halas and P. Nordlander, *Nat. Nanotechnol.*, 2015, **10**, 25–34.
- 22 A. S. Kostyukov, A. E. Ershov, V. S. Gerasimov, S. A. Filimonov, I. L. Rasskazov and S. V. Karpov, *J. Quant. Spectrosc. Radiat. Transfer*, 2019, **236**, 106599.
- 23 G. Baffou, P. Berto, E. B. Ureña, R. Quidant, S. Monneret, J. Polleux and H. Rigneault, *ACS Nano*, 2013, **7**, 6478–6488.

- 24 A. D. Phan, T.-L. Phan and L. M. Woods, *J. Appl. Phys.*, 2013, **114**, 214306.
- 25 K. Hashimoto, K. Wasada, N. Toukai, H. Kominami and Y. Kera, *A*, 2000, **136**, 103.
- 26 A. E. Ershov, V. S. Gerasimov, A. P. Gavriluyuk and S. V. Karpov, *Appl. Phys. B: Lasers Opt.*, 2017, **123**, 182.
- 27 A. P. Gavriluyuk and S. V. Karpov, *Appl. Phys. B: Lasers Opt.*, 2009, **97**, 163–173.
- 28 A. Gavriluyuk and S. Karpov, *Appl. Phys. B: Lasers Opt.*, 2011, **102**, 65–72.
- 29 A. Ershov, A. Gavriluyuk, S. Karpov and P. Semina, *Appl. Phys. B: Lasers Opt.*, 2014, **115**, 547–560.
- 30 A. Alabastri, A. Toma, M. Malerba, F. De Angelis and R. Proietti Zaccaria, *ACS Photonics*, 2015, **2**, 115–120.
- 31 Y. Ji, W. Xu, N. Ding, H. Yang, H. Song, Q. Liu, H. Ågren, J. Widengren and H. Liu, *Light: Sci. Appl.*, 2020, **9**, 1–12.
- 32 V. I. Zakomirnyi, Z. Rinkevicius, G. V. Baryshnikov, L. K. Sørensen and H. Ågren, *J. Phys. Chem. C*, 2019, **123**, 28867–28880.
- 33 V. I. Zakomirnyi, I. L. Rasskazov, L. K. Sørensen, P. S. Carney, Z. Rinkevicius and H. Ågren, *Phys. Chem. Chem. Phys.*, 2020, **22**, 13467–13473.
- 34 R. R. Birge, *J. Chem. Phys.*, 1980, **72**, 5312–5319.
- 35 B. Thole, *Chem. Phys.*, 1981, **59**, 341–350.
- 36 L. Jensen, P.-O. Åstrand, K. O. Sylvester-Hvid and K. V. Mikkelsen, *J. Phys. Chem. A*, 2000, **104**, 1563–1569.
- 37 M. L. Olson and K. R. Sundberg, *J. Chem. Phys.*, 1978, **69**, 5400–5404.
- 38 A. Mayer, *Phys. Rev. B: Condens. Matter Mater. Phys.*, 2007, **75**, 045407.
- 39 S. Grimme, J. Antony, S. Ehrlich and H. Krieg, *J. Chem. Phys.*, 2010, **132**, 154104.
- 40 J. Wang, M. Yang, J. Jellinek and G. Wang, *Phys. Rev. A*, 2006, **74**, 023202.
- 41 J. Rodríguez, M. Baltazar-Méndez, J. Autschbach and F. Castillo-Alvarado, *Eur. Phys. J. D*, 2013, **67**, 6.
- 42 E. Ringe, M. R. Langille, K. Sohn, J. Zhang, J. Huang, C. A. Mirkin, R. P. Van Duyne and L. D. Marks, *J. Phys. Chem. Lett.*, 2012, **3**, 1479–1483.
- 43 K. Ujihara, *J. Appl. Phys.*, 1972, **43**, 2376–2383.
- 44 F. Font and T. Myers, *J. Nanopart. Res.*, 2013, **15**, 2086.
- 45 R. Kofman, P. Cheyssac, A. Aouaj, Y. Lereah, G. Deutscher, T. Ben-David, J. Penisson and A. Bourret, *Surf. Sci.*, 1994, **303**, 231–246.
- 46 Z. S. Wu and Y. P. Wang, *Radio Sci.*, 1991, **26**, 1393–1401.
- 47 M. Otter, *Z. Phys.*, 1961, **161**, 539–549.
- 48 M. S. Daw and M. I. Baskes, *Phys. Rev. B: Condens. Matter Mater. Phys.*, 1984, **29**, 6443.
- 49 S. Plimpton, *J. Comput. Phys.*, 1995, **117**, 1–19.
- 50 LAMMPS, <http://lammps.sandia.gov>.
- 51 B. Voigtländer, S. Lehwald, H. Ibach, K. Bohnen and K. Ho, *Phys. Rev. B: Condens. Matter Mater. Phys.*, 1989, **40**, 8068.
- 52 S. Foiles, M. Baskes and M. S. Daw, *Phys. Rev. B: Condens. Matter Mater. Phys.*, 1986, **33**, 7983.
- 53 S. M. Rassoulinejad-Mousavi and Y. Zhang, *Sci. Rep.*, 2018, **8**, 2424.
- 54 W. G. Hoover, *Phys. Rev. A*, 1985, **31**, 1695.
- 55 X. Li, V. Carravetta, C. Li, S. Monti, Z. Rinkevicius and H. Ågren, *J. Chem. Theory Comput.*, 2016, **12**, 3325–3339.
- 56 S. Monti, G. Barcaro, L. Sementa, V. Carravetta and H. Ågren, *RSC Adv.*, 2017, **7**, 49655–49663.
- 57 S. Monti, G. Barcaro, L. Sementa, V. Carravetta and H. Ågren, *Nano Res.*, 2018, **11**, 1757–1767.
- 58 E. J. Baerends, *et al.*, *Theoretical Chemistry*, Amsterdam, 2019, pp. 931–967.
- 59 G. Ouyang, Z. M. Zhu, W. G. Zhu and C. Q. Sun, *J. Phys. Chem. C*, 2010, **114**, 1805–1808.
- 60 S. Inasawa, M. Sugiyama and Y. Yamaguchi, *J. Phys. Chem. B*, 2005, **109**, 3104–3111.
- 61 P. Schlexer, A. B. Andersen, B. Sebok, I. Chorkendorff, J. Schiøtz and T. W. Hansen, *Part. Part. Syst. Charact.*, 2019, **36**, 1800480.
- 62 G. Guisbiers, *Adv. Phys.: X*, 2019, **4**, 1668299.
- 63 W. Luo, K. Su, K. Li, G. Liao, N. Hu and M. Jia, *J. Chem. Phys.*, 2012, **136**, 234704.
- 64 J. Lee, T. Tanaka, J. Lee and H. Mori, *CALPHAD: Comput. Coupling Phase Diagrams Thermochem.*, 2007, **31**, 105–111.
- 65 P. Buffat and J.-P. Borel, *Phys. Rev. A*, 1976, **13**, 2287–2298.
- 66 P. Peng, A. Hu, A. P. Gerlich, G. Zou, L. Liu and Y. N. Zhou, *ACS Appl. Mater. Interfaces*, 2015, **7**, 12597–12618.
- 67 P. Grammatikopoulos, M. Sowwan and J. Kioseoglou, *Adv. Theory Simul.*, 2019, **2**, 1900013.
- 68 J. Ziman, *Electrons and Phonons*, Oxford University Press, 2001.
- 69 M. Liu, M. Pelton and P. Guyot-Sionnest, *Phys. Rev. B: Condens. Matter Mater. Phys.*, 2009, **79**, 035418.
- 70 A. E. Ershov, A. P. Gavriluyuk and S. V. Karpov, *Plasmonics*, 2015, **11**, 403–410.
- 71 A. Alabastri, S. Tuccio, A. Giugni, A. Toma, C. Liberale, G. Das, F. D. Angelis, E. D. Fabrizio and R. P. Zaccaria, *Materials*, 2013, **6**, 4879–4910.
- 72 M. Ferrera, M. Magnozzi, M. Canepa and F. Bisio, *J. Phys. Chem. C*, 2020, **124**, 17204–17210.
- 73 G. González-Rubio, A. Guerrero-Martínez and L. M. Liz-Marzán, *Acc. Chem. Res.*, 2016, **49**, 678–686.
- 74 H. Reddy, U. Guler, A. V. Kildishev, A. Boltasseva and V. M. Shalae, *Opt. Mater. Express*, 2016, **6**, 2776–2802.
- 75 V. S. Gerasimov, A. E. Ershov, A. P. Gavriluyuk, S. V. Karpov, H. Ågren and S. P. Polyutov, *Opt. Express*, 2016, **24**, 26851.
- 76 V. S. Gerasimov, A. E. Ershov, S. V. Karpov, A. P. Gavriluyuk, V. I. Zakomirnyi, I. L. Rasskazov, H. Ågren and S. P. Polyutov, *Opt. Mater. Express*, 2017, **7**, 799.
- 77 A. E. Ershov, A. P. Gavriluyuk, S. V. Karpov and P. N. Semina, *Chin. Phys. B*, 2015, **24**, 047804.
- 78 A. E. Ershov, V. S. Gerasimov, I. L. Isaev, A. P. Gavriluyuk and S. V. Karpov, *Chin. Phys. B*, 2020, **29**, 037802.
- 79 M. Ferrera, G. D. Valle, M. Sygletou, M. Magnozzi, D. Catone, P. O’Keeffe, A. Paladini, F. Toschi, L. Mattera,

- M. Canepa and F. Bisio, *ACS Photonics*, 2020, **7**, 959–966.
- 80 C. Noguez, *J. Phys. Chem. C*, 2007, **111**, 3806–3819.
- 81 L. K. Sørensen, A. D. Utyushev, V. I. Zakomirnyi, V. S. Gerasimov, A. E. Ershov, S. P. Polyutov, S. V. Karpov and H. Ågren, *J. Phys. Chem. C*, 2021, **125**, 13900–13908.
- 82 K. G. Thomas, in *Surface Plasmon Resonances in Nanostructured Materials*, John Wiley & Sons, Ltd, 2007, ch. 6, pp. 185–218.
- 83 N. G. Bastús, J. Comenge and V. Puntès, *Langmuir*, 2011, **27**, 11098–11105.
- 84 J. Piella, N. G. Bastús and V. Puntès, *Chem. Mater.*, 2016, **28**, 1066–1075.
- 85 S. Link and M. A. El-Sayed, *J. Phys. Chem. B*, 1999, **103**, 4212–4217.
- 86 S. Karimi, A. Moshaii, S. Abbasian and M. Nikkhah, *Plasmonics*, 2019, **14**, 851.